mater.scichina.com link.springer.com Published online 15 April 2024 | https://doi.org/10.1007/s40843-023-2867-6

Enhanced photovoltaic performance of A–D–A′–D–A type non-fused ring electron acceptors *via* side chain engineering

Xia Zhou[1,2†], Wenkui Wei[2†], Shuting Pang[2†], Xiyue Yuan[2], Junyu Li[3*], Fei Huang[2], Yong Cao[2] and Chunhui Duan[2*]

ABSTRACT **Featuring simplified synthesis and flexible chemical alteration, non-fused ring electron acceptors (NFREAs) are the ideal candidates for constructing low-cost organic solar cells (OSCs). Herein, we report three A–D–A'–D–A type NFREAs, namely ffBTz-BO, ffBTz-EH, and ffBTz-C4, where difluorinated benzotriazole (ffBTz) with different side chain lengths were employed as the weak electron-deficient A' core. Compared with ffBTz-BO and ffBTz-C4, ffBTz-EH with appropriate side chain length strikes a balance between the enhanced molecular crystallinity and the favorable face-on orientation, resulting in high charge mobilities. Consequently, ffBTz-EH-based OSC delivered the highest power conversion efficiency (PCE) of 12.96% enabled by its efficient charge transport and most suitable phase separation, which represents one of the highest efficiencies among A–D–A'–D–A type NFREAs. This work demonstrates that alkyl side chain on the central A' core plays a critical role in tuning molecular crystallinity, active layer morphology, and further device performance, which provides a meaningful perspective for designing highly efficient A–D–A'–D–A type non-fused ring electron acceptors in the future.**

Keywords: organic solar cells, non-fused ring electron acceptors, side chain engineering, molecular orientation, power conversion efficiency

INTRODUCTION

As a promising renewable energy technology, organic solar cells (OSCs) have attracted considerable attention due to their low-cost, light-weight, and flexibility [1–6]. In conventional OSCs, the bulk-heterojunction (BHJ) active layer consisting of mixed donor and acceptor materials can provide a nanoscale morphology for effective exciton dissociation and charge transport [7,8]. Owing to the rapid development of A–D–A and A–DA'D–A type fused-ring electron acceptors, the power conversion efficiencies (PCEs) of OSCs have exceeded over 19% [9–13]. However, the synthesis of A–D–A and A–DA'D–A type fused-ring electron acceptors are generally laborious, due to the complex ring closure reaction, which inevitably limits the large-scale manufacturing of OSCs [14]. As the counterparts of fused-ring electron acceptors, non-fused ring electron acceptors (NFREAs) featuring single-bond connected structures have drawn increasing attentions because of their much lower synthetic complexity and flexible chemical alteration [15–18]. At early stage, Li *et al.* [19] reported an A–D–D'–D–A type NFREA by employing difluorobenzene as the central D' core, namely DF-PCIC. It is found that the noncovalent F···H intramolecular interactions can guarantee the molecular planarity and further facilitate charge transport. However, due to the limited absorption range where the absorption onset of neat DF-PCIC film was only 781 nm, the champion device exhibited a relatively low short-circuit current density (J_{sc}) of 15.66 mA cm^{-2} and a PCE of 10.14%. Later, Chen *et al.* [20] reported an A–D–D'–D–A type NFREA, namely *o*-4TBC-2F, where four *ortho*-substituted side chains can encapsulate the central part of the planar molecular backbone. Particularly, J-aggregates were formed after thermal annealing, leading the absorption onset of the neat acceptor film to 925 nm. The corresponding OSC exhibited a much higher J_{sc} value of 20.48 mA cm^{-2}. Encouragingly, benefitting from the advanced molecular design and delicate device optimization, the PCEs of OSCs based on A–D–D'–D–A type NFREAs have achieved over 16% recently [21–23].

Apart from A–D–D'–D–A type NFREAs, to enhance the intramolecular charge transfer (ICT) effect and broaden the absorption range, A–D–A'–D–A type NFREAs have received much interest by replacing the central electron-donating D' core with the central electron-deficient A' core [24–27]. In 2020, our group developed an A–D–A'–D–A type NFREA, namely BTCIC-4Cl, by introducing benzothiadiazole (BT) as the central A' core, and successfully extended the film absorption up to 946 nm [28]. Using PBDB-T-2Cl as the polymer donor, the photovoltaic device obtained a high J_{sc} value of 21.0 mA cm^{-2}. Yet, due to the deep-lying lowest unoccupied molecular orbital (LUMO) energy level of BTCIC-4Cl, the reduced open-circuit voltage (V_{oc}) of 0.75 V resulted in a moderate PCE of 10.5%. To solve this issue, introducing a weaker electron-deficient A' core can endow NFREAs with shallow-lying LUMO level, thus a higher V_{oc}. Afterwards, Zhou *et al.* [29] reported a NFREA based on the weaker electron-deficient difluorinated benzotriazole (ffBTz) as a central A' core, namely ffBTz-HD, and the corresponding device exhibited a much higher V_{oc} of 0.86 V when

[1] School of New Energy, Ningbo University of Technology, Ningbo 315336, China
[2] Institute of Polymer Optoelectronic Materials and Devices, State Key Laboratory of Luminescent Materials and Devices, South China University of Technology, Guangzhou 510640, China
[3] Molecular Materials and Nanosystems & Institute for Complex Molecular Systems, Eindhoven University of Technology, 5600 MB Eindhoven, Netherlands
† These authors contributed equally to this work.
* Corresponding authors (emails: lijy.sshy@sinopec.com (Li J), duanchunhui@scut.edu.cn (Duan C))

pairing with PM6. However, the fill factor (FF) of 62.6% limited the device performance (10.56%) to some extent.

Compared with other molecular design strategies, side chain engineering can provide a more effective and straightforward approach to regulating the molecular crystallinity, further affecting the charge transport, FF value, and device efficiency [30]. This strategy has been successfully employed in many highly efficient small molecular acceptors [31–34]. For example, Ma *et al.* [35] designed two ladder-type FREAs with different alkyl side chain length and found the molecular orientation of thin film could be altered from edge-on (*n*-cetyl-modified) to face-on (2-hexyldecyl-modified). Generally, face-on orientation is conducive to the vertical carrier transport, thus yielding the A–D–A type fused-ring electron acceptor M3 (2-hexyldecyl-modified) with an outstanding FF value (0.76) and a power conversion efficiency of 16.66%. Furthermore, Zhang *et al.* [36] developed an A–D–A'–D–A type NFREA, namely NoCA-5, by introducing an additional *n*-octyl side chain into cyclopentadithiophene (CPDT) unit. Different from the reference acceptor NoCA-1 (without *n*-octyl side chain), NoCA-5 exhibited the enhanced intermolecular π–π stacking, smaller Urbach energy, and a more favorable phase separation. Consequently, the corresponding OSC obtained a certified PCE of 14.5% with an improved FF value from 61.7% (NoCA-1) to 72.6% (NoCA-5). Therefore, cooperated with the strategy of side chain engineering, it possesses a huge potential for difluorinated benzotriazole (ffBTz) building block to develop more efficient NFREAs.

In this work, we rationally designed and synthesized three A–D–A'–D–A type NFREAs by utilizing ffBTz as the central A' core, where the alkyl side chains on benzotriazole have been systematically altered from BO (2-butyloctcyl substitution), to EH (2-ethylhexyl substitution). It is revealed that not only the chain length but also the chain type on benzotriazole could largely affect the photovoltaic performance [37]. Thus, to explore the potential of NFREA, ffBTz-C4 with linear *n*-butyl substitution was further included, as shown in Fig. 1a. We then investigated their optoelectronic properties, photovoltaic performance, as well as the morphological characteristics. Grazing incidence wide-angle X-ray scattering (GIWAXS) results revealed that shortening side chain length could not only enhance the molecular crystallinity but also affect the orientation of thin film. Among them, ffBTz-EH, with a relatively strong crystallinity, exhibited the most favorable face-on orientation. Accordingly, by blending with the polymer donor PM6, the ffBTz-EH-based OSC delivered one of the highest PCE (12.96%) among A–D–A'–D–A type NFREAs, with simultaneously enhanced J_{sc} (21.4 mA cm^{-2}) and FF value (69.7%), which is contributed to the faster charge transport, less charge recombination, and the formation of interpenetrated fibrous networks of the active layer.

RESULTS AND DISCUSSION

Synthesis and characterization

The synthetic routes of ffBTz-BO, ffBTz-EH, and ffBTz-C4 are shown in Scheme S1 [29,38]. The critical intermediates compound **3a**–**3c** were prepared *via* direct arylation coupling with the catalyst of $Pd_2(dba)_3$. The organotin-free synthesis not only affords higher atom economy but also is more environmentally benign, which is promising for the future large quantity synthesis and large-scale device manufacturing. Subsequently, Knoevenagel condensations under mild conditions were carried out, giving the three target NFREAs. The molecular structures and purities of the key intermediates and the target NFREAs were fully characterized by ^{1}H NMR, ^{13}C NMR, and matrix-assisted laser desorption/ionization time-of-flight (MALDI-TOF) mass spectrometry (Figs S1–S18). All three NFREAs displayed good solubilities in common organic solvents, such as chloroform (> 15 mg mL^{-1}). Thermogravimetric analysis (TGA) demonstrates good thermal stabilities of ffBTz-BO, ffBTz-EH, and ffBTz-C4 (Fig. S19 and Table S1), with thermal decomposition temperatures (T_d, 5% weight loss) of 354, 353, and 350°C,

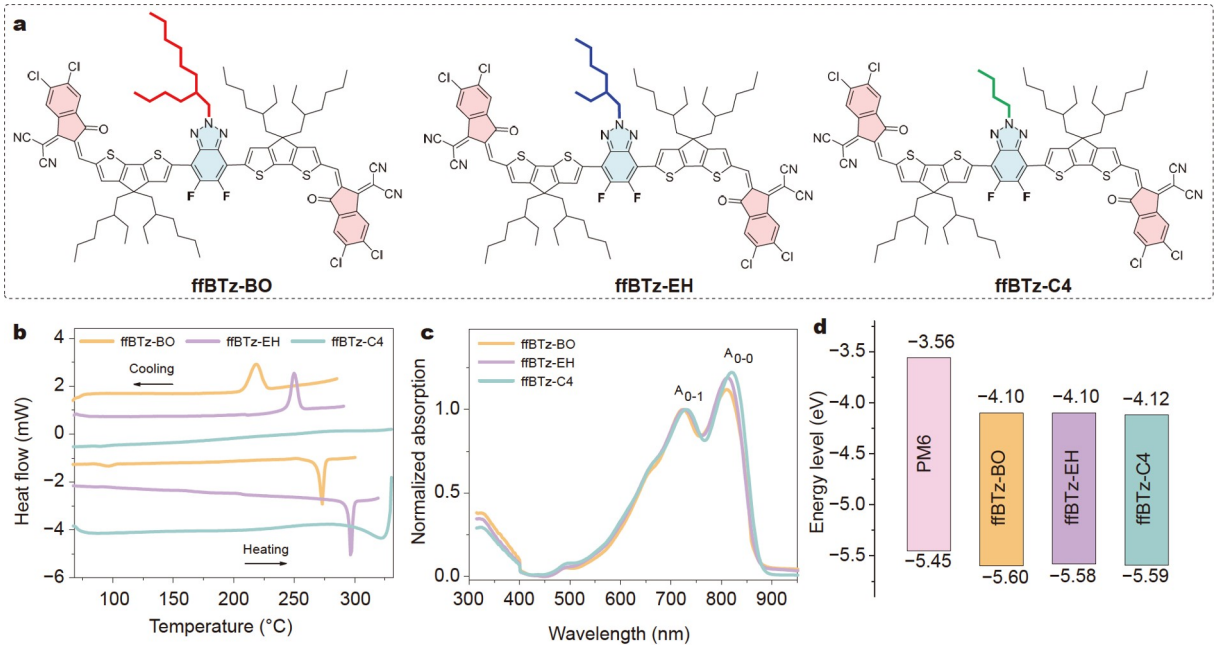

Figure 1 (a) Chemical structures, (b) DSC curves, and (c) film absorption spectra of ffBTz-BO, ffBTz-EH, and ffBTz-C4. (d) Energy level diagrams of PM6 and the three NFREAs.

respectively. To explore their phase transition behaviors, differential scanning calorimetry (DSC) analysis was performed (Fig. 1b). During the heating process, the melting peaks at 273 and 296°C were observed for ffBTz-BO and ffBTz-EH, respectively. The melting enthalpies (ΔH_ms) were increased from 42.6 J g^{-1} of ffBTz-BO to 53.2 J g^{-1} ffBTz-EH. Additionally, the crystallization peaks were also appeared during the cooling process, at 219°C for ffBTz-BO, and 250°C for ffBTz-EH with crystallization enthalpies (ΔH_cs) of 28.2 and 31.3 J g^{-1}, respectively. However, neither melting nor crystallization peaks were observed for ffBTz-C4, probably due to the decomposition of ffBTz-C4 before its melting. These observations indicate that shortening alkyl side chain could induce a stronger crystallinity of NFREAs.

The ultraviolet–visible–near-infrared (UV–*vis*–NIR) spectra of the NFREAs in solutions and as thin films are shown in Fig. S20 and Fig. 1c, respectively. In diluted chloroform solutions, the absorption peaks of the NFREAs all appeared at 740 nm, which suggests the alteration of alkyl side chain has a negligible effect on the electronic structure of the conjugated skeleton. In solid states, the absorption peaks were all red-shifted to over 810 nm, indicating the significantly enhanced intermolecular interactions from solutions to solid states. The absorption onsets of ffBTz-BO, ffBTz-EH, and ffBTz-C4 as thin films were determined to be 861, 862, and 867 nm, corresponding to an optical bandgap (E_g^{opt}) of 1.44, 1.44, and 1.43 eV, respectively (Table S2). Noticeably, the intensity of A_{0-0} peaks has been increased following the order of ffBTz-BO < ffBTz-EH < ffBTz-C4 in the normalized A_{0-1} absorption spectra. This observation illustrates that the molecular aggregation in solid state has been gradually enhanced as side chain length being shorter, echoing the results of DSC characterization [39,40]. Square wave voltammetry (SWV) was used to measure the energy levels. The oxidation/reduction curves are shown in Fig. S21, and the energy level diagram is presented in Fig. 1d. Although the varied side chain length, similar highest occupied molecular orbital (HOMO) and LUMO energy levels of three acceptors were determined, as −5.60/−4.10 eV (ffBTz-BO), −5.58/−4.10 eV (ffBTz-EH), and −5.59/−4.12 eV (ffBTz-C4), respectively.

Photovoltaic performance

To evaluate photovoltaic properties of the NFREAs, we fabricated OSCs with an architecture of ITO/PEDOT:PSS/active layer/PFN-Br/Ag. Due to the complementary light absorption and matched energy levels, a widely-used polymer PM6 was selected as electron donor to pair with the NFREAs [41]. The optimal devices were screened by donor/acceptor weight ratios, the type of solvent additives, thermal annealing (TA), and active layer thickness (Tables S3-S5). The current density–voltage (*J*–*V*) curves of the optimal devices are shown in Fig. 2a and the photovoltaic parameters are summarized in Table 1. The optimal OSC based on PM6:ffBTz-BO showed a PCE of 11.55% with an V_{oc} of 0.87 V, a J_{sc} of 20.85 mA cm^{-2}, and an FF of 63.4%. On the other hand, despite the slightly enhanced J_{sc} (21.42 mA cm^{-2}) and FF value (65.9%), ffBTz-C4 with the shortest side chain length, the corresponding device delivered a similar PCE of 11.74%, mainly due to the reduced V_{oc} value (0.83 V). For the PM6:ffBTz-EH-based OSC, all device parameters were simultaneously elevated, as 0.86 V for V_{oc}, 21.42 mA cm^{-2} for J_{sc}, and 69.7% for FF, finally resulting in the champion PCE of 12.96%, which is comparable to the state-of-the-art highly efficient A-D–A'–D–A type NFREA (Table S6). Noted that the devices based on ffBTz-BO and ffBTz-EH exhibited the similar V_{oc} (~ 0.86 V), while the value of ffBTz-C4-based device was decreased to 0.83 V. Therefore, we performed the energy loss (E_{loss}) analysis (Fig. S22 and Table S7) of ffBTz-C4 and ffBTz-EH to understand the intriguing observation. It is found that the inevitable energy loss above optical bandgap (ΔE_1) and the nonradiative recom-

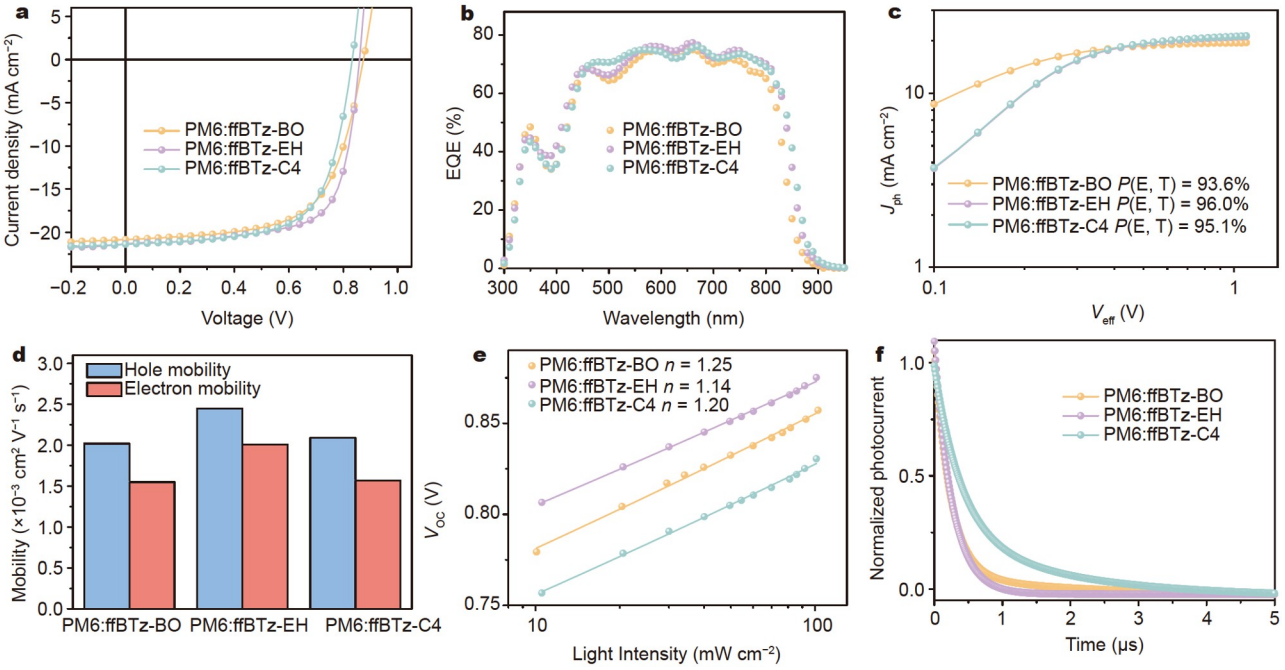

Figure 2 (a) *J*–*V* curves, (b) EQE spectra, (c) J_{ph} as a function of V_{eff} of the optimal OSCs based on ffBTz-BO, ffBTz-EH, and ffBTz-C4. (d) Hole and electron mobilities of the blend films acquired from single-carrier devices. (e) V_{oc} *versus* light intensity characteristics, (f) TPC of the optimal OSCs based on ffBTz-BO, ffBTz-EH, and ffBTz-C4.

Table 1 Photovoltaic parameters of OSCs based on ffBTz-BO, ffBTz-EH, and ffBTz-C4

Active layer	V_{oc} (V)	J_{sc}[a] (mA cm^{-2})	J_{sc} (EQE)[b] (mA cm^{-2})	FF (%)	PCE (%)
PM6:ffBTz-BO	0.87 (0.86 ± 0.01)	20.85 (20.73 ± 0.12)	20.23	63.4 (63.3 ± 0.1)	11.55 (8.68 ± 0.13)
PM6:ffBTz-EH	0.86 (0.85 ± 0.01)	21.42 (21.32 ± 0.10)	21.12	69.7 (69.5 ± 0.2)	12.96 (12.84 ± 0.12)
PM6:ffBTz-C4	0.83 (0.82 ± 0.01)	21.42 (21.29 ± 0.13)	21.01	65.9 (65.7 ± 0.2)	11.74 (11.61 ± 0.13)

a) Values in bracket were obtained from over 10 devices. b) Integrated J_{sc} from EQE spectra.

bination energy loss (ΔE_3) of both devices were similar, whereas the energy loss below optical bandgap (ΔE_2) of PM6:ffBTz-C4 was slightly lower than that of PM6:ffBTz-EH. Therefore, the overall energy loss of PM6:ffBTz-C4 is slightly lower than that of PM6:ffBTz-EH (0.575 versus 0.584 eV). However, the $qV_{oc,SQ}$, which refers to the maximum V_{oc} in a solar cell in the Shockley–Queisser limit without considering any recombination losses differs between the two devices (1.200 eV of ffBTz-EH versus 1.177 eV of ffBTz-C4). Thus, the liner *n*-butyl modified ffBTz-C4 exhibited smaller V_{oc} value. The external quantum efficiency (EQE) spectra of the OSCs are shown in Fig. 2b. All three devices gave strong and flat EQE profiles within the broad range between 450 and 850 nm. Particularly in the range of 700–800 nm, the ffBTz-EH- and ffBTz-C4-based devices achieved higher EQE response approaching 80%, which indicates more efficient photoelectron conversion processes and responsible for the higher current densities. Furthermore, the integrated current densities from the EQE spectra (J_{sc}^{EQE}) matched well with the J_{sc} values calculated from the *J*–*V* tests (within the 5% error range), which suggests good accuracy and reliability of the device metrics.

Charge generation, transfer, transport, and recombination

To verify the photon-induced charge transfer at the donor/acceptor interface, the photoluminescence (PL) emission spectra of neat and blend films were measured (Fig. S23). Under the excitation wavelength of 530 nm, the donor emissions were largely suppressed, as the quenching efficiencies over 97% for the investigated blend films, indicating that efficient electron transfer occurring from PM6 to NFREAs. When the blend films were excited at 730 nm, the acceptor quenching efficiencies were calculated to 78% for ffBTz-BO, 90% for ffBTz-EH, and 80% for ffBTz-C4, respectively. Among them, PM6:ffBTz-EH exhibited the most efficient hole transfer from acceptor to donor. The dependence of photocurrent density (J_{ph}) on effective voltage (V_{eff}) was further analyzed. Normally, J_{ph} is calculated from the equation, $J_{ph} = J_L - J_D$, where J_L and J_D represent the current densities under light and dark condition, respectively. V_{eff} is given by the equation $V_{eff} = V_0 - V_a$, where V_0 is the voltage when J_{ph} is zero, and V_a is the applied bias voltage. The exciton dissociation probability *P*(E, T) can be obtained by the J_{ph}/J_{sat} ratio under the short-circuit conditions. As shown in Fig. 2c, the *P*(E, T) of the OSCs were calculated to be 93.6% for ffBTz-BO, 96.0% for ffBTz-EH, and 95.1% for ffBTz-C4, respectively, suggesting efficient exciton dissociation in these devices.

Moreover, we employed the space-charge-limited current (SCLC) model to gain insight into the charge transport behaviors (Fig. 2d and Fig. S24) [42]. The hole mobility (μ_h) and electron mobility (μ_e) of blend films were acquired from hole-only and electron-only devices, respectively. The hole/electron mobilities of the blends were extracted to be 2.02×10^{-3}/1.55×10^{-3} for ffBTz-BO, 2.45×10^{-3}/2.01×10^{-3} for ffBTz-EH, and 2.09×10^{-3}/1.57×10^{-3} cm^2 V^{-1} s^{-1} for ffBTz-C4, and the corresponding μ_h/μ_e ratio was calculated to be 1.30, 1.22 and 1.33, respectively (Table S8). The high carrier mobilities of blend films endowed the devices with high J_{sc} values. Particularly, for PM6:ffBTz-EH system, the more balanced μ_h/μ_e ratio could mitigate space charge accumulation and thereby enhance FF value. Furthermore, the light intensity (P_{light})-dependent J_{sc} and V_{oc} measurements were conducted to understand charge recombination process of the devices [43]. The relationship between J_{sc} and P_{light} follows a power-law equation of $J_{sc} \propto P_{light}^{\alpha}$, in which the power-law factor α value close to 1 represents the negligible bimolecular recombination in the devices. As shown in Fig. S25, the PM6:ffBTz-EH-based device exhibited the highest α value of 0.995 and the most suppressed bimolecular recombination, compared with the other two devices (both α values were 0.980). On the other hand, the correlation between V_{oc} and P_{light} is described as $V_{oc} \propto (nkT/q)\ln(P_{light})$, where *k*, *T*, and *q* represent the Boltzmann constant, the Kelvin temperature, and the elementary charge, respectively. The V_{oc} versus $\ln(P_{light})$ characteristics are displayed in Fig. 2e. Generally, the slope close to kT/q indicates the dominating mechanism of bimolecular recombination, while the slope close to $2kT/q$ means the device would be prone to the trap-assisted recombination. The slope values fitted from Fig. 2e are 1.25, 1.14, and 1.20 for PM6:ffBTz-BO, PM6:ffBTz-EH and PM6:ffBTz-C4, respectively, suggesting trap-assisted charge recombination was all suppressed in these devices. Moreover, the transient photocurrent (TPC) was measured to evaluate the impact of side chain length on the extraction lifetime of charge carriers in the devices [44]. As shown in Fig. 2f, the device based on ffBTz-EH exhibited the shortest photocurrent decay time of 0.258 μs, compared with ffBTz-BO (0.416 μs) and ffBTz-C4 (0.773 μs), suggesting the most effective charge extraction capability, and echoing with the increased mobilities and reduced recombination.

Film morphology

To further verify the role of alkyl side chain and get deeper understanding of the morphology, GIWAXS was employed to characterize the crystalline behaviors in thin films. The corresponding two-dimensional scattering patterns and the one-dimensional line-cut profiles are displayed in Fig. 3 [45]. The numerical data are summarized in Table S9. For neat acceptor films, the (010) diffraction peaks in out-of-plane (OOP) direction are located at 1.74 Å^{-1} for ffBTz-BO, 1.75 Å^{-1} for ffBTz-EH,

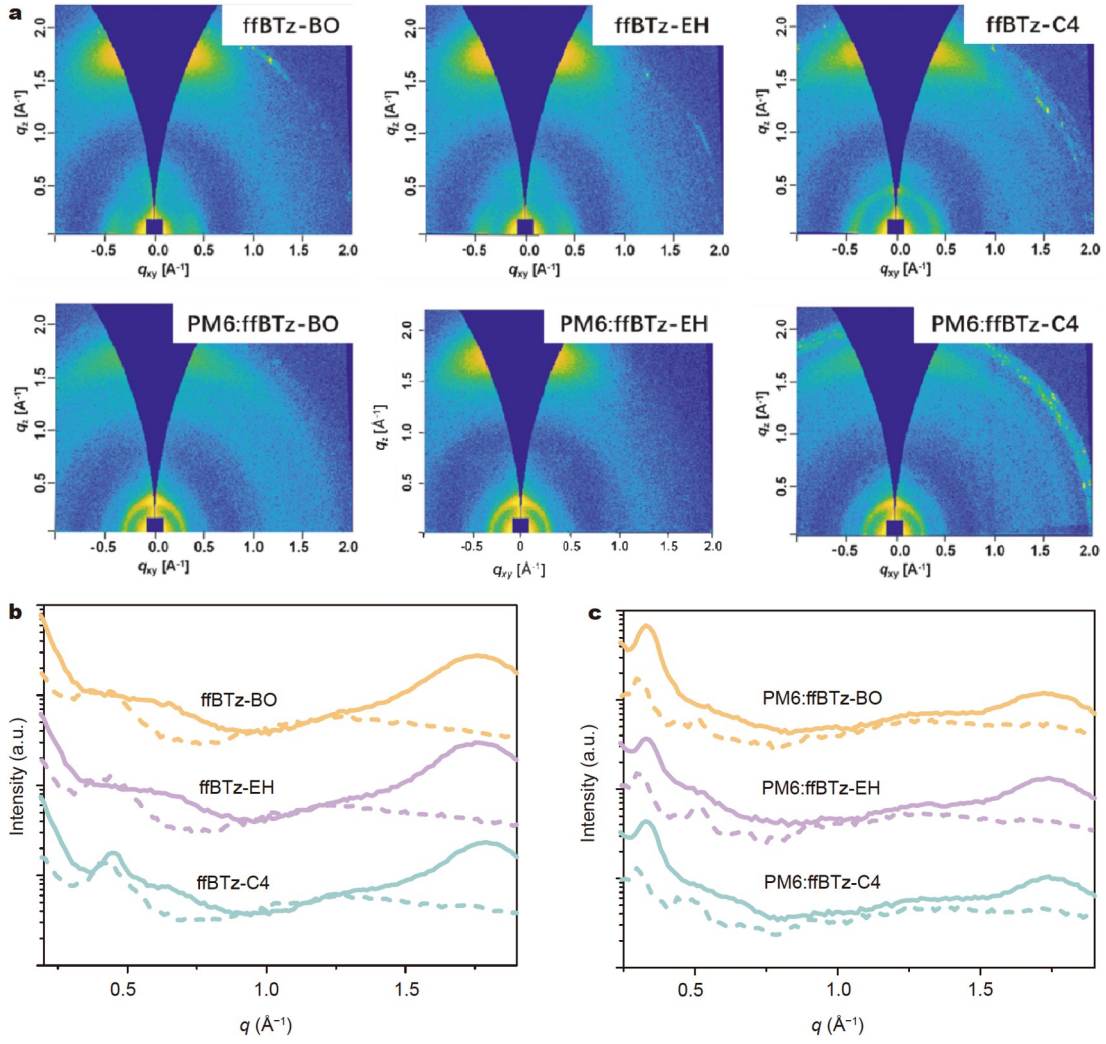

Figure 3 (a) Two-dimensional GIWAXS patterns of neat and blend films. (b, c) One-dimensional GIWAXS line-cut profiles of neat (b) and blend films (c). For the line-cut profiles, solid line depicts out-of-plane morphology and dashed line depicts in-plane film morphology.

and 1.79 Å^{-1} for ffBTz-C4, corresponding to the gradually reduced π–π stacking distances ($d_{\pi-\pi}$) of 3.61, 3.59, and 3.51 Å, respectively. Moreover, the crystal coherence lengths (CCLs) for the (010) diffraction peaks in the OOP direction are calculated to be 19.41 Å for ffBTz-BO and 20.09 Å for ffBTz-EH according to Scherrer equation, indicative of the more compact and more ordered intermolecular packing after shortening the branched side chain length. When the side chain type was changed to linear *n*-butyl, ffBTz-C4 neat film exhibited the highest value of 23.06 Å. Intriguingly, it is noteworthy that besides the (010) diffraction peaks, the ffBTz-C4 neat film appeared a (100) diffraction peak (located at 0.44 Å^{-1}) in OOP direction. Thus, different from the shortening of branched side chain length where the neat films based on ffBTz-BO and ffBTz-EH adopted similar face-on molecular orientation relative to the substrate, the mixed face-on and edge-on orientation were coexisted in ffBTz-C4 neat film after the side chain type was changed from branched to linear one. Further, the electron mobilities of neat acceptor films were characterized (Fig. S26). It is indicated that the highest electron mobility (4.61×10^{-3} cm^2 V^{-1} s^{-1}) was achieved in ffBTz-EH neat film. On the other hand, despite the strongest crystallinity, the linear chain modified ffBTz-C4 exhibited slightly lower value (4.11×10^{-3} cm^2 V^{-1} s^{-1}), which might be attributed to the mixed molecular orientation. The neat PM6 film was also characterized (Fig. S27), in which a (100) diffraction peak (q = 0.33 Å^{-1}) in OOP direction was recorded, suggesting a mixed orientation (face-on and edge-on coexisted). After blending with PM6, the alkyl side chain engineering has varied effect on three NFREAs. All blend films exhibited pronounced (100) diffraction peaks at 0.33 Å^{-1} in OOP direction, which should belong to the lamellar stacking of PM6. For (010) diffraction peaks in OOP direction, ffBTz-BO-based blend film showed relatively weakened diffraction intensity (located at 1.72 Å^{-1}). We attributed this to its intrinsic weak crystallinity of ffBTz-BO, thus the face-on orientation is prone to being disturbed after the introduction of polymer donor. When the side chain length continues to decrease, the more pronounced (010) diffraction peaks in OOP direction revealed that the acceptor packing has been preserved at maximum extent in PM6:ffBTz-EH system, and keeping the strong face-on orientation in blend film. The face-on orientation in thin film is essential for solar cells to improve the vertical charge transport within the active layer, as evidenced by the effective charge dynamics analysis. On the other hand, due to the mixed orientation in neat film, the

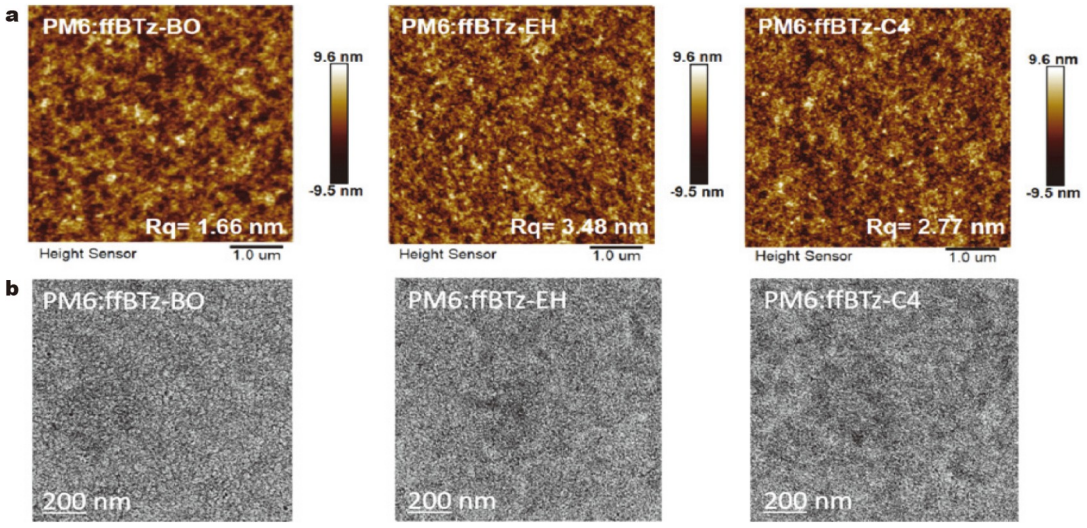

Figure 4 (a) AFM height images, and (b) TEM images of PM6:ffBTz-BO, PM6:ffBTz-EH, and PM6:ffBTz-C4 blend films.

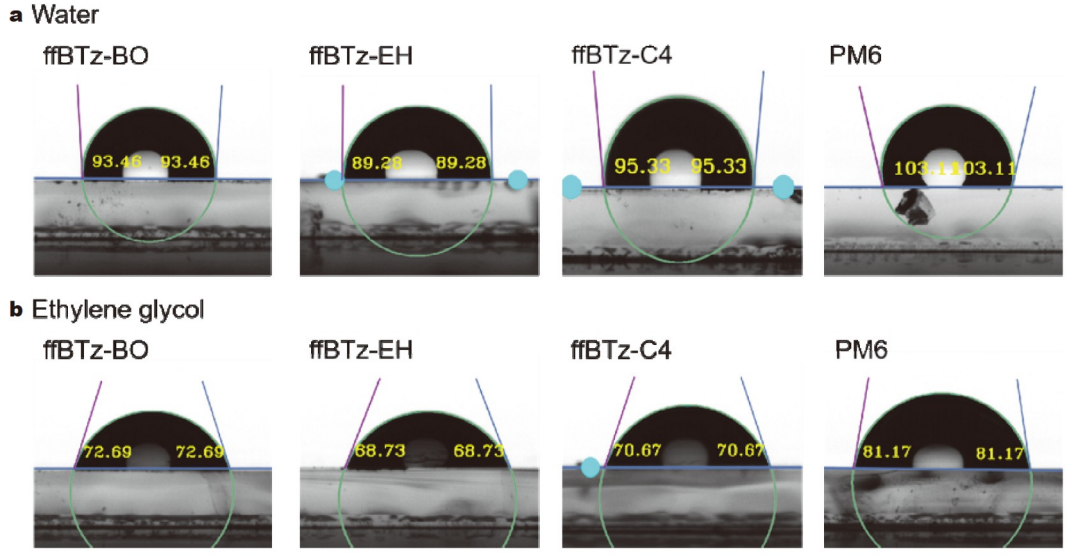

Figure 5 Contact angles of water (a) and ethylene glycol (b) on the neat films of ffBTz-BO, ffBTz-EH, ffBTz-C4, and PM6.

intensity of (010) diffraction peaks in OOP direction is becoming weaker in PM6:ffBTz-C4 blend film, suggesting the suppression of face-on orientation.

Furthermore, we investigated the nanoscale separation morphology of active layer using atomic force microscopy (AFM) and transmission electron microscopy (TEM). As shown in Fig. 4a, the ffBTz-BO-based blend film exhibited a relatively smooth surface with root mean square (RMS) surface roughness of 1.66 nm, indicating good miscibility with polymer PM6. Whereas larger RMS values, as 3.48 nm for ffBTz-EH and 2.77 nm for ffBTz-C4, are presented, mainly due to the stronger crystallinities of the electron acceptors. In TEM images (Fig. 4b), PM6:ffBTz-BO exhibited smaller grain, while PM6:ffBTz-EH and PM6:ffBTz-C4 blend films afforded more suitable nanoscale phase separation along with the more interpenetrated fibrous networks, which is conducive to exciton dissociation as well as charge transport. From the above results, it is observed that the morphological evolution has been occurred by fine-tuning alkyl side chain length. Among them, ffBTz-EH, with a middle chain length, possesses a proper crystallinity, predominant face-on orientation, and suitable phase separation, which is beneficial for charge transport in the vertical direction, thus giving rise to the superior FF value and champion PCE.

Furthermore, contact angle and surface energy (γ) measurements were conducted to investigate the miscibility of between polymer donor and acceptors (Fig. 5). As summarized in Table S10, the γ values of ffBTz-BO, ffBTz-EH, ffBTz-C4 neat films are 32.44, 34.96, and 34.84 mN m^{-1}, respectively. According to the empirical equation $\chi = K\left(\sqrt{\gamma_D} - \sqrt{\gamma_A}\right)^2$, where K is a positive constant, γ_D and γ_A refer to the surface energies of donor and NFREA neat films, the Flory–Huggins interaction parameters (χ) were calculated to be 0.33, 0.63 and 0.61 for PM6 blended with ffBTz-BO, ffBTz-EH, and ffBTz-C4, respectively. The smallest χ value suggests the increased miscibility between PM6 and ffBTz-BO, which explained the smaller surface roughness in AFM

results. On the other hand, the higher χ values of PM6:ffBTz-EH and PM6:ffBTz-C4 blends indicate the higher domain purity, which is beneficial for charge collection and suppressing charge recombination, thus resulting in higher FF.

CONCLUSIONS

In summary, three A–D–A'–D–A type NFREAs, namely ffBTz-BO, ffBTz-EH, and ffBTz-C4, were designed and synthesized to systematically investigate the influence of alkyl chain length on the photoelectric, morphological, and photovoltaic properties. By shortening the alkyl side chain length, the crystallinity and molecular orientation of NFREAs were successfully manipulated. Particularly, ffBTz-EH, with an appropriate chain length and chain type, strikes a balance and possesses not only a strong crystallinity but also a favorable face-on orientation of thin films. As a result, the photovoltaic device based on PM6:ffBTz-EH presents one of the highest PCEs (12.96%) among A–D–A'–D–A type NFREAs, with simultaneously improved J_{sc} and FF, which benefits from its effective charge dynamics and suitable film morphology. This work emphasizes the critical role of alkyl side chain in fine-tuning the crystallinity, molecular packing, and active layer morphology of A–D–A'–D–A type NFREAs to construct high-performance and low-cost OSCs in the future.

Received 29 December 2023; accepted 12 March 2024; published online 15 April 2024

1 Cheng P, Li G, Zhan X, *et al.* Next-generation organic photovoltaics based on non-fullerene acceptors. Nat Photon, 2018, 12: 131–142
2 Inganäs O. Organic photovoltaics over three decades. Adv Mater, 2018, 30: 1800388
3 Cui C, Li Y. High-performance conjugated polymer donor materials for polymer solar cells with narrow-bandgap nonfullerene acceptors. Energy Environ Sci, 2019, 12: 3225–3246
4 Fukuda K, Yu K, Someya T. The future of flexible organic solar cells. Adv Energy Mater, 2020, 10: 2000765
5 Liu Y, Liu B, Ma CQ, *et al.* Recent progress in organic solar cells (Part I material science). Sci China Chem, 2021, 65: 224–268
6 Zhang G, Lin FR, Qi F, *et al.* Renewed prospects for organic photovoltaics. Chem Rev, 2022, 122: 14180–14274
7 Yu G, Gao J, Hummelen JC, *et al.* Polymer photovoltaic cells: Enhanced efficiencies *via* a network of internal donor-acceptor heterojunctions. Science, 1995, 270: 1789–1791
8 Zhu L, Zhang M, Zhong W, *et al.* Progress and prospects of the morphology of non-fullerene acceptor based high-efficiency organic solar cells. Energy Environ Sci, 2021, 14: 4341–4357
9 Lin Y, Wang J, Zhang ZG, *et al.* An electron acceptor challenging fullerenes for efficient polymer solar cells. Adv Mater, 2015, 27: 1170–1174
10 Yuan J, Zhang Y, Zhou L, *et al.* Single-junction organic solar cell with over 15% efficiency using fused-ring acceptor with electron-deficient core. Joule, 2019, 3: 1140–1151
11 Zheng Z, Wang J, Bi P, *et al.* Tandem organic solar cell with 20.2% efficiency. Joule, 2022, 6: 171–184
12 Zhu L, Zhang M, Xu J, *et al.* Single-junction organic solar cells with over 19% efficiency enabled by a refined double-fibril network morphology. Nat Mater, 2022, 21: 656–663
13 Yao H, Hou J. Recent advances in single-junction organic solar cells. Angew Chem Int Ed, 2022, 61: e202209021
14 Li X, Pan F, Sun C, *et al.* Simplified synthetic routes for low cost and high photovoltaic performance *n*-type organic semiconductor acceptors. Nat Commun, 2019, 10: 519
15 Yang M, Wei W, Zhou X, *et al.* Non-fused ring acceptors for organic solar cells. Energy Mater, 2022, 1: 100008
16 Shen Q, He C, Li S, *et al.* Design of non-fused ring acceptors toward high-performance, stable, and low-cost organic photovoltaics. Acc Mater Res, 2022, 3: 644–657
17 Mishra A, Sharma GD. Harnessing the structure-performance relationships in designing non-fused ring acceptors for organic solar cells. Angew Chem Int Ed, 2023, 62: e202219245
18 Luo D, Brabec CJ, Kyaw AKK. Non-fused ring electron acceptors for high-performance and low-cost organic solar cells: Structure-function, stability and synthesis complexity analysis. Nano Energy, 2023, 114: 108661
19 Li S, Zhan L, Liu F, *et al.* An unfused-core-based nonfullerene acceptor enables high-efficiency organic solar cells with excellent morphological stability at high temperatures. Adv Mater, 2018, 30: 1705208
20 Chen YN, Li M, Wang Y, *et al.* A fully non-fused ring acceptor with planar backbone and near-IR absorption for high performance polymer solar cells. Angew Chem Int Ed, 2020, 59: 22714–22720
21 Ma DL, Zhang QQ, Li CZ. Unsymmetrically chlorinated non-fused electron acceptor leads to high-efficiency and stable organic solar cells. Angew Chem Int Ed, 2023, 62: e202214931
22 Wang X, Zeng R, Lu H, *et al.* A simple nonfused ring electron acceptor with a power conversion efficiency over 16%. Chin J Chem, 2023, 41: 665–671
23 Li D, Zhang H, Cui X, *et al.* Halogenated nonfused ring electron acceptor for organic solar cells with a record efficiency of over 17%. Adv Mater, 2023, 36: 2310362
24 Miao J, Meng B, Liu J, *et al.* An A-D-A'-D-A type small molecule acceptor with a broad absorption spectrum for organic solar cells. Chem Commun, 2018, 54: 303–306
25 Liu X, Wei Y, Zhang X, *et al.* An A-D-A'-D-A type unfused nonfullerene acceptor for organic solar cells with approaching 14% efficiency. Sci China Chem, 2021, 64: 228–231
26 Deng S, Zhang L, Zheng J, *et al.* A simple fused-ring acceptor toward high-sensitivity binary near-infrared photodetector. Adv Opt Mater, 2022, 10: 2200371
27 Luo D, Jiang Z, Tan WL, *et al.* Non-fused ring acceptors achieving over 15.6% efficiency organic solar cell by long exciton diffusion length of alloy-like phase and vertical phase separation induced by hole transport layer. Adv Energy Mater, 2023, 13: 2203402
28 Pang S, Zhou X, Zhang S, *et al.* Nonfused nonfullerene acceptors with an A-D-A'-D-A Framework and a benzothiadiazole core for high-performance organic solar cells. ACS Appl Mater Interfaces, 2020, 12: 16531–16540
29 Zhou X, Pang S, Wu B, *et al.* Noncovalent interactions induced by fluorination of the central core improve the photovoltaic performance of A-D-A'-D-A-type nonfused ring acceptors. ACS Appl Energy Mater, 2022, 5: 7710–7718
30 Luo Z, Xu T, Zhang C, *et al.* Side-chain engineering of nonfullerene small-molecule acceptors for organic solar cells. Energy Environ Sci, 2023, 16: 2732–2758
31 Jiang K, Wei Q, Lai JYL, *et al.* Alkyl chain tuning of small molecule acceptors for efficient organic solar cells. Joule, 2019, 3: 3020–3033
32 Ye L, Weng K, Xu J, *et al.* Unraveling the influence of non-fullerene acceptor molecular packing on photovoltaic performance of organic solar cells. Nat Commun, 2020, 11: 6005
33 Cui Y, Yao H, Zhang J, *et al.* Single-junction organic photovoltaic cells with approaching 18% efficiency. Adv Mater, 2020, 32: 1908205
34 Zhang Z, Wang H, Yu J, *et al.* Modification on the indacenodithieno [3,2-*b*]thiophene core to achieve higher current and reduced energy loss for nonfullerene solar cells. Chem Mater, 2020, 32: 1297–1307
35 Ma Y, Zhang M, Wan S, *et al.* Efficient organic solar cells from molecular orientation control of M-series acceptors. Joule, 2021, 5: 197–209
36 Zhang X, Li C, Qin L, *et al.* Side-chain engineering for enhancing the molecular rigidity and photovoltaic performance of noncovalently fused-ring electron acceptors. Angew Chem Int Ed, 2021, 60: 17720–17725
37 Qi F, Jones LO, Jiang K, *et al.* Regiospecific *N*-alkyl substitution tunes the molecular packing of high-performance non-fullerene acceptors. Mater Horiz, 2022, 9: 403–410
38 Price SC, Stuart AC, Yang L, *et al.* Fluorine substituted conjugated polymer of medium band gap yields 7% efficiency in polymer-fullerene

solar cells. J Am Chem Soc, 2011, 133: 4625–4631
39 Clark J, Silva C, Friend RH, *et al.* Role of intermolecular coupling in the photophysics of disordered organic semiconductors: Aggregate emission in regioregular polythiophene. Phys Rev Lett, 2007, 98: 206406
40 Spano FC. The spectral signatures of Frenkel polarons in H- and J-aggregates. Acc Chem Res, 2010, 43: 429–439
41 Zhang M, Guo X, Ma W, *et al.* A large-bandgap conjugated polymer for versatile photovoltaic applications with high performance. Adv Mater, 2015, 27: 4655–4660
42 Blakesley JC, Castro FA, Kylberg W, *et al.* Towards reliable charge-mobility benchmark measurements for organic semiconductors. Org Electron, 2014, 15: 1263–1272
43 Kyaw AKK, Wang DH, Gupta V, *et al.* Intensity dependence of current-voltage characteristics and recombination in high-efficiency solution-processed small-molecule solar cells. ACS Nano, 2013, 7: 4569–4577
44 Street RA, Song KW, Northrup JE, *et al.* Photoconductivity measurements of the electronic structure of organic solar cells. Phys Rev B, 2011, 83: 165207
45 Mahmood A, Wang JL. A review of grazing incidence small- and wide-angle X-ray scattering techniques for exploring the film morphology of organic solar Cells. Sol RRL, 2020, 4: 2000337

Acknowledgements The research received financial support from the Ministry of Science and Technology of China (2019YFA0705900), National Natural Science Foundation of China (U20A6002, 22275058, and 22109046), Guangdong Innovative and Entrepreneurial Research Team Program (2019ZT08L075), Guangdong Basic and Applied Basic Research Foundation (2022B1515120008), and the Start-up Founding Research and Cultivation Project funded by Ningbo University of Technology (2022KQ65 and 2022TS03).

Author contributions Zhou X synthesized the electron acceptors and conducted the characterization; Zhou X and Wei W performed the data analysis. Pang S performed the photovoltaic device fabrication and characterization. Yuan X synthesized the polymer donor. Li J performed the GIWAXS measurements and data analysis. Huang F and Cao Y participated in project administration. Duan C conceived the idea and supervised the project. Zhou X, Wei W, and Duan C prepared the manuscript. All authors contributed to the general discussion.

Conflict of interest The authors declare no competing interests.

Supplementary information Experimental details and supporting data are available in the online version of the paper.

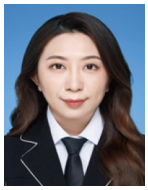

Xia Zhou received her PhD degree in materials science and engineering from the South China University of Technology. She is currently a lecturer at Ningbo University of Technology. Her current research focuses on the design and synthesis of non-fullerene acceptors, molecular packing analysis and organic solar cells.

Wenkui Wei is currently a PhD candidate in the South China University of Technology under the supervision of Prof. Chunhui Duan. He received his bachelor and master degrees from Dalian University of Technology in 2018 and 2021. His main research interest is the design and synthesis of non-fullerene acceptors and applications in organic solar cells.

Shuting Pang received her PhD degree from the South China University of Technology in 2020. She is currently an associate professor at Hangzhou Dianzi University. Her current research interests include organic solar cells and perovskite solar cells.

Chunhui Duan received his BS degree from Dalian University of Technology in 2008 and PhD degree from the South China University of Technology in 2013. After a postdoc training at Eindhoven University of Technology, he joined the South China University of Technology as a full professor in 2017. His research interests focus on organic optoelectronic materials and their applications in solar cells, photodetectors, and transistors.

通过侧链工程提高A–D–A’–D–A型非稠环电子受体的光伏性能

周霞[1,2†], 魏文魁[2†], 庞淑婷[2†], 袁熙越[2], 李俊宇[3*], 黄飞[2], 曹镛[2], 段春晖[2*]

摘要 非稠环电子受体(NFREA)具有合成简单和结构修饰灵活的特点, 是制备高性能低成本有机太阳电池(OSCs)的理想材料. 本工作以不同侧链修饰的二氟苯并三氮唑(ffBTz)作为弱缺电子核(A’), 分别设计合成了三种A–D–A’–D–A型NFREA, 即ffBTz-BO、ffBTz-EH和ffBTz-C4. 其中, ffBTz-EH, 由于其合适的侧链长度, 在分子结晶度和分子堆积优势取向之间取得了平衡, 从而获得了更高的电荷迁移率. 并且得益于高效的电荷传输和最合适的相分离形貌, 基于ffBTz-EH的OSC获得12.96%的最高能量转换效率, 这也是A–D–A’–D–A型NFREA获得的最高效率之一. 本研究表明, A’核心上的烷基侧链在调节分子结晶度、活性层形貌和进一步调控器件性能方面起着至关重要的作用, 这为未来设计高效低成本的A–D–A’–D–A型非稠环电子受体提供了思路.